JPMTR 088 | 1608
DOI 10.14622/JPMTR-1608
UDC 620.1|531-3:678.5

Research paper
Received: 2016-08-11
Accepted: 2016-12-16

Mechanical properties of 3D printed polymers

Azem Yahamed[1], Pavel Ikonomov[2], Paul D. Fleming[1], Alexandra Pekarovicova[1], Peter Gustafson[3], Arz Qwam Alden[3] and Saif Alrafeek[3]

[1] Department of Chemical and Paper Engineering,
Western Michigan University, Kalamazoo, MI 49008

[2] Department of Engineering Design Manufacturing,
and Management Systems,
Western Michigan University, Kalamazoo, MI 49008

[3] Department of Mechanical Engineering,
Western Michigan University, Kalamazoo, MI 49008

E-mails: azemkhalifa.yahamed@wmich.edu
pavel.ikonomov@wmich.edu
dan.fleming@wmich.edu
a.pekarovicova@wmich.edu

Abstract

Polymeric bone implants are used in many medical applications. To create bone structures from plastics that can match the real bones, the structure and mechanical properties must be tested to make sure they can sustain loads comparable to the original. Also, it is very important to use proper materials that provide biocompatibility. In this work, the mechanical properties of 3D printed samples of thermoplastic materials that can be used for 3D printing of human bone structure substitutes were tested. The thermoplastics that were printed using 3D printing are acrylonitrile butadiene styrene (ABS), Digital ABS™, polylactic acid (PLA), polyetherimide ULTEM 9085 and polyamide PA 2200. The samples of ABS and PLA were printed using fused deposition modeling technology (FDM), Digital ABS™ was printed using PolyJet™ technology, and ULTEM 9085 and PA 2200 were printed using selective laser sintering (SLS). Compression tests showed that PLA and Digital ABS™ create anisotropic 3D printed structures, because they exhibited different stress vs. strain properties in different directions. The samples made from ABS, ULTEM9085 and PA2200 have the same shape of stress-strain curves in different printing directions, but different slopes, which shows that these printed structures are also anisotropic. Differential scanning calorimetry was used to acquire the thermal analysis profile of these polymers. The thermal analysis results of these polymers indicate that ABS and ULTEM9085 are amorphous while PLA is partially crystalline and PA2200 is completely crystalline.

Keywords: polymeric material, fused deposition modeling, bone structure, 3D model, selective laser sintering

1. Introduction

The goal of this work is to design and build bone structures from biocompatible plastic materials and investigate their mechanical properties. We studied and tested several biocompatible materials to investigate the possibility of their use in bone structures by using three-dimensional (3D) printing. Replicating of the bone structures is a complex process of imaging, design and fabrication of replacement tissue, which has been the subject of several studies in recent years.

1.1 Building bone structures

Initially, image slices of bones according to digital imaging and communications in medicine (DICOM) standard are acquired using magnetic resonance imaging (MRI) or computed tomography (CT) scans from actual body organs. Next, 3D modeling software is used to produce a new part or the model of the missing bone structure. The 3D model is then imported into 3D printing software for building the substitute bone structure (Leukers et al., 2005). Recently, there have been many successful attempts to 3D print items for human bone substitutes, using 3D printing technology (Ehrenberg, 2013a; 2013b).

1.2 Thermoplastics

Thermoplastics have been used successfully as replacements for certain metals for many years in manufacturing and have been used widely in medical applications

(Jia and Kagan, 2001; Lasprilla et al., 2012). In applying these materials, 3D printing has a significant role, providing high performance, cost efficiency and enhanced resistance to environmental conditions. The low melting temperature used in 3D printing is considered an advantage of the technology to create high quality parts for manufacturing and in medical applications, also allowing precise manufacturing for replacement of tissue, specifically bone structures.

1.3 Fused Deposition Modeling

Fused Deposition Modeling (FDM) is a method widely used to produce 3D printed items from thermoplastics (Ahn et al., 2002; Materialise, 2016a). The first step is to create a 3D model and then convert it to STL (stereolithography) file format to produce the 3D object. This format has some advantages and disadvantages. The advantage of STL format is that it facilitates the geometry of the object by reducing it to its initial components and it can maintain and adjust the geometry of 3D model such as shape and size. The disadvantage of STL format is that the object loses some of its resolution because it uses only triangles to represent the complex geometry. Once the STL file format is imported to the 3D printing software to be prepared for 3D printing, it is sliced into numerous thin slices that become layers during the 3D printing process.

These layers define the two-dimensional planes that the 3D printing process will produce to build the 3D object. When created, the layers are stacked upon one another, thus creating a 3D object directly from the original design. It is obvious that the thinner the layer is, and higher the precision is of the 2D movement, the higher is the precision that can be carried out for an item (Hutmacher, 2000). The working mechanism of the FDM technique is that it takes a plastic filament from a coil and drives it through an extruder. The plastic is heated and melted by the heat extrusion nozzle, the molten filament flows through the nozzles, and is deposited on the building plate to form a layer. The heads move on the X-Y axes to follow a predefined path to form a specific shape on each layer. Then, the platform moves vertically in the Z direction to produce the next layer (Hutmacher, 2000). Three-dimensional printing with thermoplastics is one of the most common methods to create 3D structures in both medical and industrial fields (Fischer, 2011).

1.4 Selective Laser Sintering

Selective Laser Sintering (SLS) is another rapid prototyping process that can manufacture 3D structures directly from 3D models. Applying laser sintering technology, objects are built layer by layer (Materialise, 2016b). The method uses a high-power laser to fuse tiny particles of powders, such as plastic, metal, ceramic and glass, into a structure that has a desired 3D form. The principle of SLS process is that a thin layer of powder is distributed and leveled by a roller above the flat surface. Then, a laser beam follows a defined profile on the layer and melts the powder that bonds together. To make room for the new layer of powder, the piston in the cylinder shifts down by one layer thickness.

Next, the powder supply piston goes up to provide a fresh amount of powder for the subsequent layer. The powder is distributed again on the flat surface. The laser repeats the same process as on the first layer. This process repeats layer by layer until the entire object is built. The SLS technique is capable of producing objects from an extensive variety of powder materials. These materials can contain polymers, such as nylon or polystyrene, or metals, such as steel, titanium, alloy mixtures and green sand. In addition, materials that can be used are polyamide, glass filled polyamide and alumide, a combination of aluminum and polyamide (Materialise, 2016b; Palermo, 2013).

For medical purposes, SLS has been used for making bone tissue engineering builds for sites, such as temporomandibular joint using polycaprolactone, since it provides a technique to build scaffolds to match the anatomical geometry of periodontal structures. The method allows building scaffolds with complicated inner and outer structures (Williams et al., 2005).

1.5 Stereolithography

Stereolithography is a developed process using a container of liquid UV-curable monomer and a UV laser to construct layers. For each layer, the laser ray draws a cross-section of the part model on the surface of the liquid resin. When the resin is cured by the laser beam it solidifies; after movement in the X-Y direction following the layer pattern, the layer of the model is created and bonds to the lower layer. When the laser ray hits the surface of the liquid monomer, the photopolymer is created, which rapidly hardens. After one layer is totally drawn, the stage is lowered one step down into the container and the second layer will be sketched on top of the first. The material bonds every layer to the prior one, repeating the process over-and-over again till it builds the entire shape of the 3D part. Stereolithography is a fast method that has a high level of precision and good finishing properties (Materialise, 2016c).

1.6 PolyJet technology

PolyJet™ technology (Stratasys, 2016a) is a manufacturing process that can produce smooth, exact parts with a layer resolution of 16 μm and precision of 0.1 mm height. The process can produce thin walls and complex geometric shapes with many materials. PolyJet 3D printing jets layers of curable liquid photopolymer

onto a build substrate, which is like inkjet printing that fires drops of ink onto paper. The build preparation software automatically estimates the placement of photopolymers and support material from a 3D CAD file. The 3D printer jets and directly UV-cures small drops of liquid prepolymer. The adherent layers gather on the build substrate to generate an accurate 3D model. The 3D printer jets a removable gel like support material when the complex shapes are in need for support. Then, the support material can be removed easily by the operator's hand or flushing with water. PolyJet 3D printing technology can offer several advantages for rapid prototyping. The technology can make smooth detailed prototypes, produce complex shapes, complicated details and smooth surfaces. In addition, it can combine color and various material properties into one model with the best material versatility obtainable.

2. Methods

2.1 Three-dimensional printing of test samples

We used SolidWorks software to design and create 3D models for tensile test, compressive test and bending test samples with specific dimensions according to the MTS published standards (MTS, 2014; 2015a). Then, using 3D printing technology five different 3D printed samples of polymeric materials were printed, with five replicates for each sample for each test: acrylonitrile butadiene styrene (ABS) (Test Standard Labs, 2016), polylactic acid (PLA) (MakeItFrom, 2015), polyetherimide ULTEM9085 (Stratasys, 2016b), polyamide PA2200 (EOS, 2015), and Digital ABS™, an acrylic photopolymer, (Stratasys, 2016c). Although ABS is not biocompatible material, it is used as a reference for comparison with other polymers. Polylactic acid is a biopolymeric material that can be used in the human body. The polymer has great biocompatibility and mechanical properties, and, because of these features, is widely used in tissue engineering (Lasprilla et al., 2012). A study was performed to evaluate the biocompatibility of the prepared polyetherimide (PEI) by using osteoblast cell line MG63. The results of the research by Tao and Young (2006) showed the PEI was helpful as a tissue engineering scaffold for bone regeneration. PA2200 is biocompatible and it can be used in several medical applications. For instance, compressed structures for scaffold supporting, soft tissue and osseous augmentation are used in neural implants (Stoia, Vigaru and Rusu, 2015).

Selected mechanical and physical properties of these materials are shown in Table 1.

To make 3D printing objects, 3D models need to be created in advance; 3D slicer and OsiriX software were used to design 3D models that were then converted to STL format for 3D printing. The sample size and dimensions can be controlled as needed. Parameters of 3D printing, such as temperature, extruder speed, infill percentage (100–0 % volume), temperature of the heated plate and resolution can be also controlled. Figure 1 shows the 3D printer running while printing the test sample.

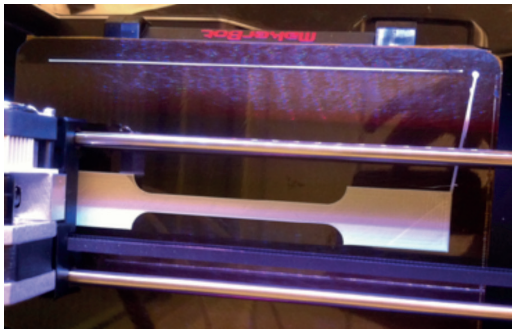

Figure 1: 3D printing tensile test sample on MakerBot

2.2 Testing mechanical properties of 3D printed samples using MTS test system

After printing 3D samples for tensile tests, compression tests and bending tests, we tested the samples using MTS Bionix Servohydraulic Test Systems Model 370.02. The force capacity of the device is 25 kN and it is used to determine the quasistatic mechanical proper-

Table 1: Selected properties of polymeric materials from the material safety data sheets (MSDS)

Material	Tensile strength (MPa)	Young modulus (MPa)	Melting point (°C)
ABS	44.8	2 250	100*
PLA	57.8	3 500	160
ULTEM9085	71.6	2 200	186
PA2200	48.0	1 700	172–180
Digital ABS™	60.0	2 600–3 000	47–53*

* Melting temperature is replaced by the glass transition temperature (*Tg*) for ABS and Digital ABS™, since these materials cannot be crystallized.

ties for a number of biomaterials. The axial alignments of the system are intended to achieve precise tension, compression and bending tests as well as fatigue and fracture studies. Also, they are used to test durability properties of components such as hip, knee and spine implants (MTS, 2015b).

The tested samples were designed according to the MTS standards with specific dimensions for all mechanical property tests. We tested the 3D printed samples at 0.2 mm/s speed of the MTS machine at room temperature.

2.3 Creating of 3D bone structure model using OsiriX

OsiriX is a free open-source software used to create 3D models of human organs from CT, MRI and ultrasound scans. These provide high quality images used for different medical applications including surgeries. To create 3D models for 3D printing bone structures, DICOM images from CT and MRI were acquired by obtaining information from actual patients (Ikonomov and Yahamed, 2014).

For creating 3D models, there are several steps required. The initial step is that the region of interest (ROI) must be selected on each image. After that, the segmentation should be performed to separate the borders of the organ. An example of using OsiriX to make the 3D model is shown in Figure 2. OsiriX enables to view, approximate, read and post process the images, with the techniques for 2D imaging, database, and 3D models.

Figure 2 illustrates the collection of images used to describe the ROI and segmentation, (highlighted in green color), to create the 3D model. Once the segmentation is finished through all the slides, the volumization is carried out to create the final 3D shape. As shown in Figure 3, the 3D model is visualized by OsiriX. Then the model is exported to 3D format, which is STL in our case, to be printed by a 3D printer. The mechanical properties of the 3D printed samples can be tested, once the samples for the MTS test machine are printed at ambient temperature.

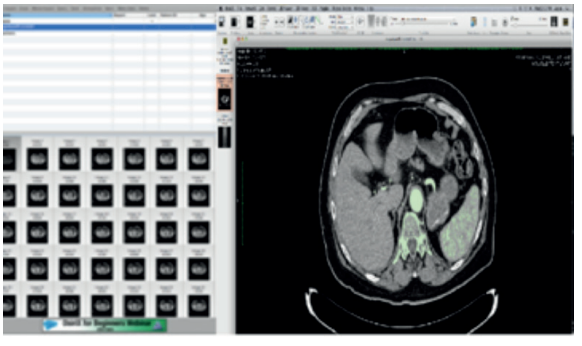

Figure 2: Region of interest and segmentation in OsiriX

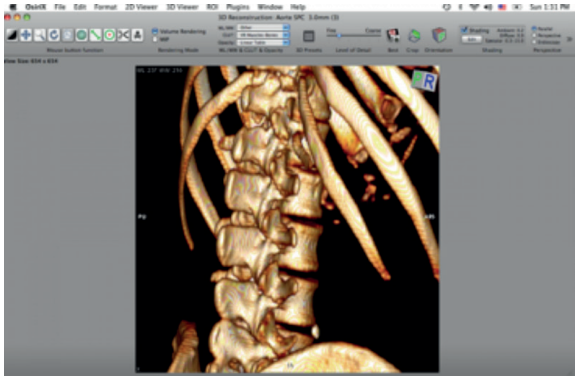

Figure 3: 3D model created after segmentation in OsiriX

2.4 Cleaning 3D model using MeshLab

Before 3D printing, the mesh model needs to be cleaned and smoothened. We used MeshLab software for cleaning of the mesh, which means removing all the tiny geometrical irregularities that may be found in shell meshes. Common problems that usually occur in the model are duplicated vertices, unreferenced null faces, self-intersecting faces, non-manifold faces and small holes. For filling holes, we use the hole filler tool that allows us to select holes and edit them in different ways. The basic filling algorithm uses a technique that inserts a face between the two adjacent border edges. This algorithm selects every time the best pair of adjacent border edges into the hole. Then smoothing of the model is performed, as shown in Figure 4 (Yahamed, Ikonomov and Fleming, 2014). A bone structure sample was printed to test the accuracy of the 3D printer as shown in Figure 5. For that, 3D models were exported to STL format to be printed by the 3D printer (MakerBot replicator 2X).

2.5 Thermal analysis by Differential Scanning Calorimetry

Differential Scanning Calorimetry (DSC) was used to investigate the amorphous and crystalline behavior of these polymers. This tool is important in thermal analysis to investigate how the enthalpy of materials is changed by temperature. A sample with known weight is heated or cooled and the changes in its heat capacity are tracked as changes in the heat flow. This can detect transitions, such as glass transition temperatures and melting temperatures (Pekarovicova, Chovancova-Lovell and Fleming, 2006). Test samples of 0.045 g for all polymers were used. For the first cycle, the sample was held for 1 min at 35 °C, then it was heated from 35 °C to 260 °C at 10 °C/min. After that, it was held for 1 min at 260 °C and cooled from 260 °C to 35 °C at 60 °C/min. The same steps were repeated for the second cycle for all the samples. These analyses indicate how the polymers behave after reheating and recooling.

Figure 4: 3D model of vertebra cleaned by MeshLab software

Figure 5: 3D printed bone vertebra structure

3. Results and discussion

3.1 Tensile strength tests

Five different polymeric materials were printed and tested using the MTS machine. The FDM technique was used to print ABS, PLA and ULTEM9085 polymeric materials (see Table 1 for selected properties). The SLS method was used to print one polymeric material PA2200. PolyJet Technology was used to print Digital ABS™. Five samples were printed for each material. All the samples were printed as a solid at 100 % of infill. We used an MTS machine to test the tensile strength, compression and bending of the 3D printed polymeric specimens. Specific equations were used to calculate stress and strain for each test. Figure 6 shows the stress-strain curves of the materials, calculated by least squares regression of the experimental data using a quadratic polynomial at 100 % infill and the MTS machine speed of 0.2 mm/s at room temperature for tensile test.

The equation regressed to the stress-strain data is of the form

$$\sigma = E\varepsilon + F\varepsilon^2 \qquad [1]$$

where σ is the stress, ε is the strain and E is Young's modulus. The coefficient of the squared term, F is negative for convex curves and positive for concave curves (Boyd and Vanderberghe, 2004; Weisstein, 2016). The fits were regressed in Minitab™ with no intercept. Comparison of measured and fit data are given in the Appendix.

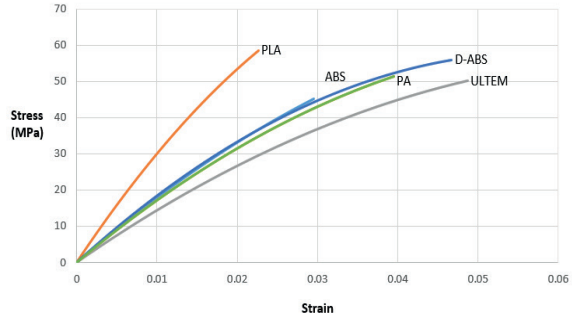

Figure 6: Tensile stress-strain calculated from least squares fit to tensile data for the materials

The shapes of stress-strain curves pinpoint brittle structures, which do not exhibit any dramatic change in elongation prior to rupture. Beer et al. (2012) reported that brittle material ruptures without any obvious prior change in the rate of elongation.

Table 2 shows the results of the tensile strength and Young's modulus after testing with the MTS machine. By making a comparison between the results of the tensile strength of 3D printed samples, and the values of the material safety data sheet (MSDS) from the manufacturer, both measured tensile strength and Young's modulus values were slightly less than the ones provided by the manufacturer, which was most likely due to repeated heating and extrusion of the tested polymeric samples. For PA2200 that was printed by SLS they were indistinguishable from the values obtained from the manufacturer.

Table 2: The values and standard deviations of tensile strength and Young's modulus of the polymers at 100 % infill after testing with MTS machine

Material	Tensile strength (MPa)	SD (MPa)	Young's modulus (MPa)	SD (MPa)
ABS	44.0	2.0	1 925	29
PLA	57.0	2.0	3 333	18
ULTEM9085	49.7	0.6	1 540	3
PA2200	49.7	0.7	1 699	12
Digital ABS™	55.0	3.0	2 013	12

From Table 2, PLA has the highest values for both Young's modulus and tensile strength. After that, Digital ABS™ has the second highest values for both Young's modulus and tensile strength. On the other hand ULTEM9085 has the lowest value for Young's modulus and ABS has the lowest value for tensile strength. Cortical bones have a compressive strength in the range of 131–224 MPa, and a Young's modulus ranging from 17 000–20 000 MPa, while compressive strength and Young's modulus for trabecular bones are 5–10 MPa and 50–100 MPa, respectively (Razak, Sharif and Raman, 2012). The strength and modulus of the polymers are less than the criteria of the compact bone, but they exceed the criteria of the trabecular bone.

Table 3 shows the breaking energy per unit mass and energy per unit mass absorbed per unit strain for the polymers at 100 % infill. Here, PA2200 has the highest values for both tensile breaking energy per unit mass and energy per unit mass absorbed for unit strain (121 kJ/kg and 3951 kJ/kg), respectively.

3.2 Compressive tests

Figures 7 and 8 show the stress-strain curves calculated (from least square fits to compression stress-strain data, using equation similar to Equation 1) at 100 % infill for compression tests in X and Z directions accordingly, while Figure 9 shows the stress-strain curves and calculated (from regression fits to equation similar to Equation 1) at 100 % infill for bending tests. The comparison of fits to raw data are given in the Appendix.

Compression tests give information about the compressive properties of the material of interest. The specimen dimensions were printed according to the standard, and they can be either blocks or cylinders for this test – in our case we made them blocks with the specific dimensions according to ASTM D695 (ASTM International, 2015a). The compressive test properties explain the performance of the material when it is compressed under a load that is relatively low and uniform. The equations used to calculate stress and strain for compressive tests are the same as for tensile tests.

Figures 7 and 8 show the relation between stress vs. strain and the fitted points of the samples for each material. For ABS polymer, the curves appear convex as in Figure 7, when the material was printed horizontally along the X axis, and in Figure 8 when it was printed vertically in the Z axis, but the slopes are not the same in both printing directions. This indicates that this material creates anisotropic 3D printed structures, because it has different slopes in different printing directions. Table 4 shows the values of the compressive strength and compressive modulus for selected materials from MSDS.

For PLA, when it was printed along the X axis, the curve appears convex, while it appears concave when it was printed perpendicularly along the Z axis. This indicates that PLA created anisotropic 3D printed structures, since it has different behavior in different printing directions.

Table 3: Density and the values and standard deviations of breaking energy per unit mass and energy per unit mass absorbed per unit strain for the polymers at 100 % infill

Material	Density (kg/m^3)	Breaking energy per unit mass (kJ/kg)	SD (kJ/kg)	Energy per unit mass absorbed per unit strain (kJ/kg)	SD (kJ/kg)
ABS	1.04×10^3	42.0	2.0	1 851	28
PLA	1.25×10^3	46.0	2.0	2 666	14
ULTEM9085	1.34×10^3	37.3	0.4	1 149	2
PA2200	0.43×10^3	121.0	2.0	3 951	28
Digital ABS™	1.18×10^3	47.0	3.0	1 706	10

Table 4: Compressive strength and compressive modulus for selected materials from MSDS

Material	Compressive strength (MPa)	Compressive modulus (MPa)
ABS	65	2 500
PLA	80	4 000
ULTEM9085	104	1 930
PA2200	58	1 500
Digital ABS™	110	2 200

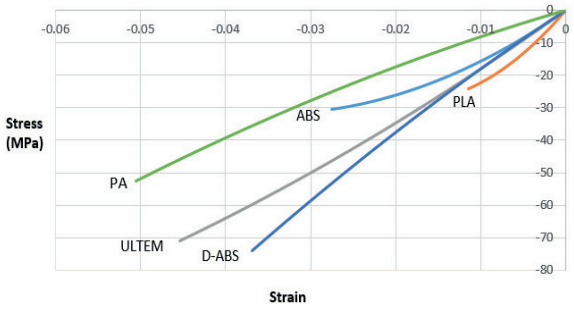

Figure 7: Compressive stress-strain calculated from fits at 100 % infill for the materials in X direction

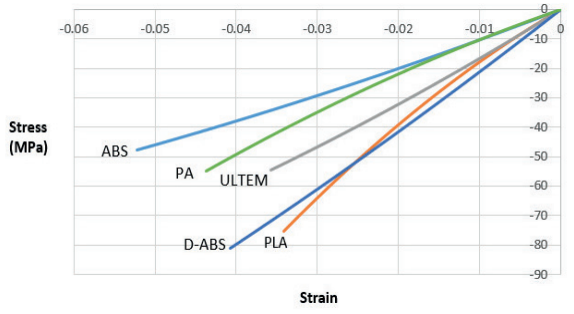

Figure 8: Compressive stress-strain calculated from fits at 100 % infill for the materials in Z direction

The same behavior was found with Digital ABS™, which was printed by using PolyJet™ technology. When it was printed along the X axis, the curve appears concave, while it appears convex when it was printed vertically along the Z axis. This indicates Digital ABS™ also creates anisotropic 3D printed structures.

The rest of the materials showed the same behavior in both directions (Figures 7 and 8). For ULTEM9085 the curves were convex, while for PA2200 the curves were concave in both printing directions; but the slopes are different in both printing directions for both materials. This is an indicator that ULTEM9085 and PA2200 also form anisotropic 3D printed structures. All of these materials have in common that they are thermoplastic polymers, which means that they form linear polymeric chains, thus it can be expected, that the strength is highest in the direction of polymeric chains, and in other directions the strength will be lower.

Table 5 shows the results of compressive strength and compressive modulus after testing with the MTS machine. The table shows the results of the polymeric samples that were printed at 100 % of infill along both directions X and Z for compression tests. It is obvious that the values of the compressive modulus and compressive strength of the tested samples are lower than the original values from the MSDS (Table 4). It was found that for compressive modulus the values of the concave figures are less than the values of the convex figures regardless the printing direction, but if the figures have the same shape in both printing directions, then the values of the compressive modulus of the samples that were printed vertically along the Z axis are less than the ones that were printed horizontally along the X axis and vice versa for the compressive strength.

From Table 5, PLA has the highest compressive modulus in the X direction and the second highest compressive strength in the Z direction. Digital ABS™ has

Table 5: The values and standard deviations of compressive strength and compressive modulus after testing with MTS machine

Material	Print Direction	Compressive strength (MPa)	SD (MPa)	Compressive modulus (MPa)	SD (MPa)
ABS	X	30.0	2.00	1 839	12
ABS	Z	45.0	7.00	1 055	20
PLA	X	24.7	0.60	3 077	29
PLA	Z	74.8	0.30	1 610	28
ULTEM9085	X	70.0	0.05	1 870	13
ULTEM9085	Z	55.0	0.05	1 721	10
PA2200	X	51.9	0.20	1 175	23
PA2200	Z	54.9	0.20	1 064	24
Digital ABS™	X	75.0	5.00	2 157	20
Digital ABS™	Z	80.0	0.04	1 729	20

Table 6: The values and standard deviations of compressive breaking energy per unit mass and compressive energy per unit mass absorbed per unit strain for the polymers at 100 % infill

Material	Print Direction	Breaking energy per unit mass (kJ/kg)	SD (kJ/kg)	Energy per unit mass absorbed per unit strain (kJ/kg)	SD (kJ/kg)
ABS	X	29.0	2.00	1 768	11
ABS	Z	43.0	7.00	1 014	19
PLA	X	19.8	0.50	2 462	22
PLA	Z	59.8	0.20	1 288	21
ULTEM9085	X	52.2	0.04	1 396	10
ULTEM9085	Z	41.0	0.04	1 284	7
PA2200	X	120.7	0.50	2 733	51
PA2200	Z	127.7	0.50	2 474	53
Digital ABS™	X	64.0	4.00	1 828	17
Digital ABS™	Z	67.8	0.03	1 465	17

the highest compressive strength in the Z direction and the second highest compressive modulus in the X direction. On the other hand PA2200 has the lowest compressive modulus in the X direction and ABS has the lowest compressive modulus in the Z direction. The compressive modulus values of human trabecular bones range from 1 MPa to 5000 MPa, with strength values ranging from 0.10 MPa to 27.3 MPa (Williams et al., 2005). The polymers show compressive modulus values ranging from 1175 MPa to 3077 MPa when they were printed horizontally along the X axis and from 1055 MPa to 1729 MPa when they were printed vertically along the Z axis. The compressive strength values of the polymers range from 25 MPa to 75 MPa for the samples that were printed along the X axis and from 45 MPa to 80 MPa for the ones that were printed along the Z direction. The compressive modulus values fall within the range of human trabecular bone, while the compressive strength values exceed the range of human trabecular bones.

Table 6 shows the compressive breaking energy per unit mass and compressive energy per unit mass absorbed per unit strain for the polymers at 100 % infill. Here, PA2200 has the highest values for compressive breaking energy per unit mass and compressive energy per unit mass per unit strain in both printing directions X and Z.

3.3 Bending tests

Bending tests measure the force required to bend a beam under three-point loading conditions. The purpose of this test is to select materials for parts that support loads without bending. The flexural modulus indicates the stiffness of material when bent. The load is applied to the center generating three-point bending at a given rate. The test results are the support span, loading rate, and the determined deflection. They all are based on the specimen thickness and are defined by ASTM D790 (ASTM International, 2015b). The equations used to calculate bending stress and bending strain are different from those used to calculate stress and strain for tensile and compressive tests. Figure 9 shows clearly the convex shape of bending stress-strain curves for all materials except Digital ABS™, which appears concave. Table 7 shows the flexural strength and flexural modulus of the selected materials from their MSDS.

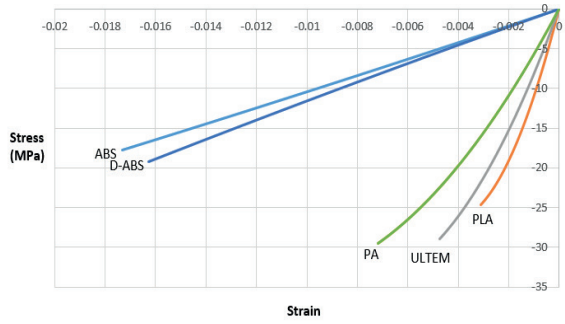

Figure 9: Stress-strain calculated from fit to bending data at 100 % infill for the material

Table 7: Flexural strength and flexural modulus for selected materials from MSDS

Material	Flexural strength (MPa)	Flexural modulus (MPa)
ABS	69	2 300
PLA	80	4 000
ULTEM9085	115	2 500
PA2200	58	1 500
Digital ABS™	66	1 700–2 200

Table 8: The values and standard deviations of flexural strength and flexural modulus after testing with MTS machine

Material	Flexural strength (MPa)	SD (MPa)	Flexural modulus (MPa)	SD (MPa)
ABS	17.6	0.9	1 063	16
PLA	25.0	2.0	2 627	20
ULTEM9085	30.0	1.0	2 049	20
PA2200	29.9	0.1	1 490	30
Digital ABS™	20.0	5.0	1 120	8

Table 9: The values an standard deviations of flexural breaking energy per unit mass and flexural energy per unit mass absorbed per unit strain for the polymers at 100 % infill

Material	Density (kg/m^3)	Breaking energy per unit mass (kJ/kg)	SD (kJ/kg)	Energy per unit mass absorbed per unit strain (kJ/kg)	SD (kJ/kg)
ABS	1.04×10^3	16.9	0.9	1 022	15
PLA	1.25×10^3	20.0	2.0	2 102	16
ULTEM9085	1.34×10^3	22.4	0.7	1 529	15
PA2200	0.43×10^3	69.8	0.2	3 465	69
Digital ABS™	1.18×10^3	17.0	4.0	949	7

Table 8 shows the results of the flexural strength and flexural modulus after testing with MTS machine. The values of the flexural modulus and flexural strength in Table 8 after testing with MTS machine are more or less decreased comparing to the values of the flexural modulus obtained from MSDS in Table 7. In Table 8 PLA has the highest flexural modulus value, after that ULTEM9085 is the second highest value and PA2200 is the third.

Table 9 shows the flexural breaking energy per unit mass and flexural energy per unit mass absorbed per unit strain for the polymers at 100 % infill. Here, PA2200 has the highest flexural breaking energy and flexural energy per unit mass absorbed at unit strain (69.8 kJ/kg and 3 465 kJ/kg), respectively. As before, these represent energies per unit mass absorbed before failure or per unit strain.

3.4 Compressive tests for ABS cubes

We designed a cube with 1 inch (25.4 mm) sides using SolidWorks for compression tests and printed several specimens of ABS using MakerBot replicator 2X as a solid at 100 % of infill. The cubes were tested in different directions X, Y, and Z at two different speeds, 0.2 mm/s and 0.05 mm/s. We tested two sets of cubes, each set containing six cubes, and each couple was tested in a different direction. After testing them with the MTS machine, we obtained two different strain regions for all the cubes – the low strain region and high strain region. The results of compressive strength and compressive modulus for low strain and high strain regions were compared with the results of the compression tests of the standard samples with the specific dimensions according to ASTM D695. The results of high strain region of ABS cubes approximately match the results of the samples having dimensions according to the standard, while the results of low strain region never match. Figure 10 shows the stress-strain curves calculated from least squares fit to compression data for ABS cubes at 100 % for the high strain region at a speed of 0.2 mm/s on the MTS machine.

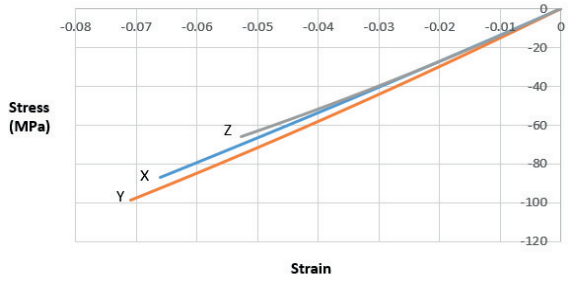

Figure 10: ABS cubes stress-strain calculated from fit at 100 % infill for high strain in X, Y, Z directions for compression speed of 0.2 mm/s

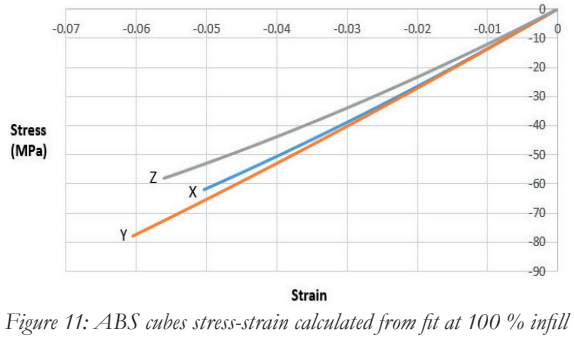

Figure 11: ABS cubes stress-strain calculated from fit at 100 % infill for high strain in X, Y, Z for compression speed of 0.05 mm/s

Table 10: The values and standard deviations of compressive strength and compressive modulus for ABS cubes for low strain region

Print Direction	Speed (mm/s)	Compressive strength (MPa)	SD (MPa)	Compressive modulus (MPa)	SD (MPa)
X	0.20	5.0	1.0	260	8
Y	0.20	6.7	0.7	248	3
Z	0.20	4.5	0.9	330	9
X	0.05	5.0	2.0	284	11
Y	0.05	5.5	0.7	206	3
Z	0.05	3.9	0.3	236	7

Table 11: The values and standard deviations of compressive strength and compressive modulus for ABS cubes for high strain region

Print Direction	Speed (mm/s)	Compressive strength (MPa)	SD (MPa)	Compressive modulus (MPa)	SD (MPa)
X	0.20	70	16.0	1 375	6
Y	0.20	90	9.0	1 373	7
Z	0.20	61	6.0	1 427	4
X	0.05	60	2.0	1 393	3
Y	0.05	70	8.0	1 396	9
Z	0.05	56	0.1	1 241	7

Figure 11 shows the stress-strain curves calculated from least squares fit to compression data for ABS cubes at 100 % infill for the high strain region at a speed of 0.05 mm/s on the MTS machine.

Tables 10 and 11 show the results of compressive strength and compressive modulus for both regions of strain (low and high, respectively) for ABS cubes when they were tested in different directions X, Y, and Z at two different speeds. The low strain moduli for the X and Y directions are indistinguishable. This should be expected based on how the MakerBot prints each layer in the X and Y directions.

3.5 Thermal analysis

To better understand melting, solidification and leveling of these thermoplastics, differential scanning calorimetry (DSC) was done. It is important to understand material behavior under the influence of thermal loads.

Thermal analysis provides important information of use to engineers and designers.

The results of thermal analysis for ABS by using DSC are shown in Figure 12. We heated the sample and then cooled it consecutively for two cycles. Figure 12 shows the behavior of ABS during the first and second cycle. A small exothermic peak appeared around 50 °C, but the graph in general indicates that ABS is an amorphous polymer.

Consequently, the thermal analysis results of PLA, ULTEM9085 and PA2200 were obtained by following the same steps using the DSC under the same conditions.

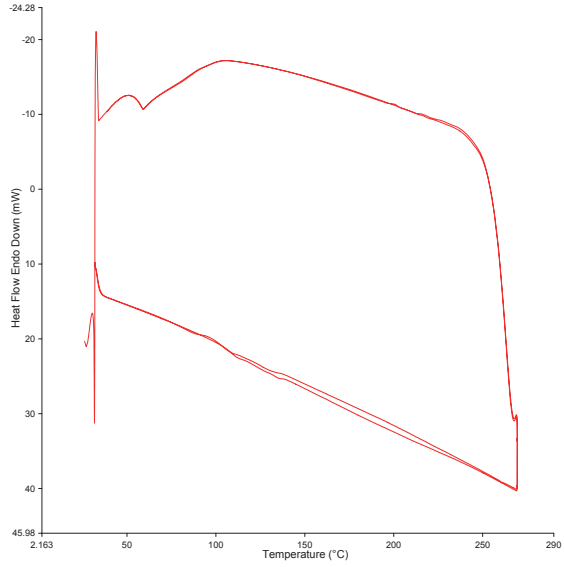

Figure 12: Thermal analysis of ABS

PLA thermal analysis, as plotted in Figure 13, shows that there are two small endothermic peaks. The first peak appeared around 60 °C, which is the *Tg* for the polymer during the first cycle while the second peak was around 160 °C, which is the melting point (*Tm*) of PLA for both cycles. This indicates the polymer is partially crystalline.

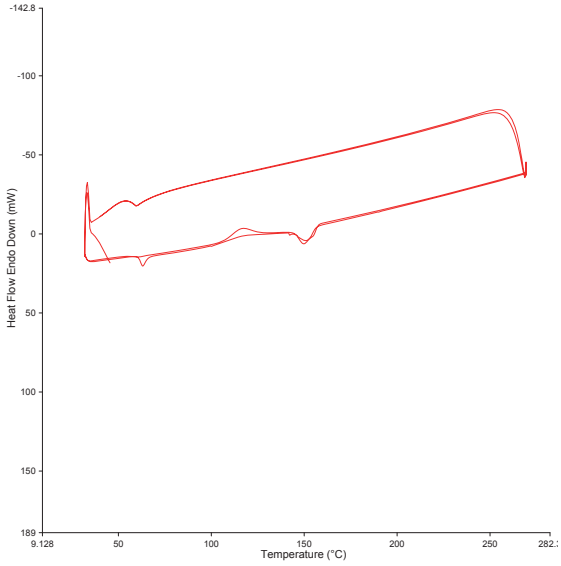

Figure 13: Thermal Analysis of PLA

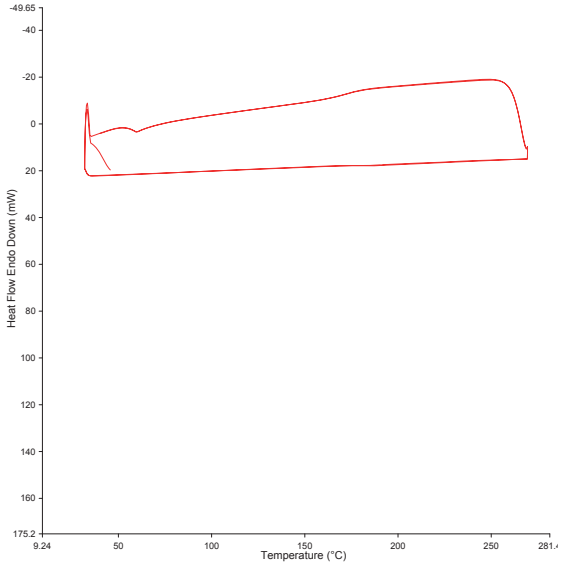

Figure 14: Thermal Analysis of ULTEM9085

ULTEM9085 thermal analysis is shown in Figure 14. From Figure 14, we can see there are no peaks appearing during the first or the second cycle and the uniform shape of the curves at the Figure 14 indicates that the ULTEM9085 is an amorphous polymer.

The thermal analysis for PA2200 is shown in Figure 15, showing two sharp peaks. The first peak was exothermic and appeared around 150 °C and the second one is endothermic around 180 °C, which is the melting point (*T*m) of PA2200. These sharp peaks appear clearly during the first and second cycle, which shows crystalline behavior of the PA2200.

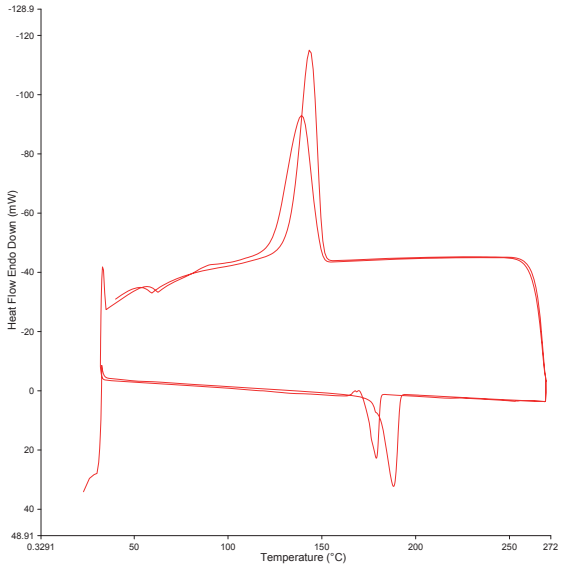

Figure 15: Thermal Analysis of PA2200

These results indicate that ABS and ULTEM can show better leveling, and hence smoother surfaces if an annealing step is included in the printing process. Annealing can be of some value for PLA, but probably is of little value for PA2200.

4. Summary and Conclusion

Five polymers, ABS, PLA, PA2200, ULTEM9085, and Digital ABS™ were printed and tested for selected properties in tensile strength tests, compressive tests and bending tests. The thermoplastic materials ABS, PLA and ULTEM 9085 were printed at 100 % of infill using FDM technology. The thermoplastic polymer PA2200 was printed using SLS technology at 100 % of infill. Digital ABS™ was printed using PolyJet™ technology. Five replicates from each material were printed and tested for each property. The average tensile strength and Young's moduli of the 3D printed samples and flexural strength properties were slightly lower than the values of the MSDS that were obtained from the manufacturer. The curves show near linear trends, showing that the rupture occurs without any dramatic change in elongation, which is typical for brittle structures.

Also, the values of the compressive modulus and compressive strength of the tested samples are lower than the original values obtained from the MSDS. This was most likely due to the heating and extrusion of the 3D printed tested samples, since they were extruded for a second time. For PA2200, which was printed using SLS, the tensile strength and Young modulus were indistinguishable from the values that obtained from the manufacturer (MSDS). Compression tests show that PLA and

Digital ABS™ are anisotropic polymers because they have different properties in different printing directions. ABS, ULTEM9085, and PA2200 have the same shape in both printing directions, but different slopes.

The highest values for both Young's modulus and tensile strength has PLA, while ULTEM9085 has the lowest Young's modulus value and ABS has the lowest tensile strength value. Further, PLA has the highest compressive modulus in the X direction and the second highest compressive strength in the Z direction. Digital ABS™ has the highest compressive strength in the Z direction and the second highest compressive modulus in X direction; PA2200 has the lowest compressive modulus in the X direction and ABS has the lowest compressive modulus value in the Z direction. Finally, PLA has the highest flexural modulus value, ULTEM9085 has the second highest value and PA2200 the third highest.

Bending tests show that all the curves of the polymers appear clearly convex except for digital ABS™ that appears concave. The values of the flexural modulus after testing with the MTS machine are less than the values of the flexural moduli obtained from the MSDS, and the values of the flexural strength after testing with the MTS machine are also less than the ones obtained from the MSDS.

The PA2200 has the highest breaking energy per unit mass for both tensile test and energy absorbed per unit mass per unit strain, 121 kJ/kg and 3 951 kJ/kg, respectively. It also has the highest values for compressive breaking energy and compressive energy absorbed per unit mass per unit strain in both printing directions X and Z. The compressive breaking energy per unit mass is 121 kJ/kg in X and 128 kJ/kg in Z direction. The compressive energies absorbed per unit mass per unit strain are 2 733 kJ/kg in X and 2 474 kJ/kg in Z direction. In addition, PA2200 has the highest flexural breaking energy and flexural energy absorbed per unit mass per unit strain, 69.8 kJ/kg and 3 465 kJ/kg, respectively.

For ABS cubes, after testing with the MTS machine, two different strain regions were obtained for all the cubes; low strain region and high strain region. The results of the high strain region of ABS cubes approximately match the results of the samples that have dimensions according to the standard ASTM D695, while the results of low strain region never match.

The thermal analyses of these polymers indicate that ABS and ULTEM9085 are amorphous, while PLA is partially crystalline and PA2200 is completely crystalline. These indicate that the ABS and ULTEM9085 can show better leveling, and hence smoother surfaces if an annealing step is included in the printing process. Annealing can be of some value for PLA, but probably is of little value for PA2200.

Regarding the results of mechanical properties, strength and modulus of the polymers of 3D printed trabecular structures are higher than the ones of the real trabecular bones. In contrast, the 3D printed compact bones show lower mechanical properties (both strength and modulus) than the real compact bones structure. We believe we can strengthen the structure and geometry to match these requirements in future work.

After reaching the best mechanical properties of the 3D printed biopolymers in a specific design that replaces the missing bony part, animal trials need to be conducted to investigate the influence of the implants on the tissue healing process. The technology of 3D printing is expanding continuously. Processing costs, including material costs, energy costs and production speed are being wisely estimated together with that involved in more conventional manufacturing processes.

References

Ahn, S.-H., Montero, M., Odell, D., Roundy, S. and Wright, P.K., 2002. Anisotropic material properties of fused deposition modeling ABS. *Rapid Prototyping Journal,* 8(4), pp. 248–257.

ASTM International, 2015a. *ASTM D695-15 Standard Test Method for Compressive Properties of Rigid Plastics*. Westconchocken, PA: ASTM International.

ASTM International, 2015b. *ASTM D790-15e2 Standard Test Method for Flexural Properties of Unreinforced and Reinforced Plastics and Electrical Insulating Materials*. Westconchocken, PA: ASTM International.

Beer, F.P., Johnston, E.R., DeWolf, J.T. and Mazurek, D.F., 2012. *Mechanics of Materials*. New York: McGraw Hill Companies.

Boyd, S.P. and Vanderberghe, L., 2004. *Convex Optimization*. New York: Cambridge University Press.

Ehrenberg, R., 2013a. Health & Illness: Skull patched with plastic. *Science News,* 183(8), p. 12.

Ehrenberg, R., 2013b. Plastic implant replaces three-quarters of man's skull. *Science News*, 11 March 2013.

EOS, 2015. *Material data sheet: PA 2200*. [pdf] EOS GmbH – Electro Optical System. Available at: <https://www.shapeways.com/rrstatic/material_docs/mds-strongflex.pdf> [Accessed September 2015].

Fischer, F., 2011. *Thermoplastics: The Best Choice for 3D Printing*. Eden Prairie, MN: Stratasys Inc.

Hutmacher, D.W., 2000. Scaffolds in tissue engineering bone and cartilage. *Biomaterials,* 21(24), pp. 2529–2543.

Ikonomov, P. and Yahamed, A., 2014. Testing of plastic materials for 3D printing of bone structure. *International Journal of Advanced Manufacturing Systems, 15*(1), pp. 23–29.

Jia, N. and Kagan, V.A., 2001. Mechanical performance of polyamides with influence of moisture and temperature – accurate evaluation and better understanding. In: J. Moalli, ed. 2001. *Plastic Failure Analysis and Prevention*. Norwich, NY: William Andrew Inc. pp. 95–104.

Lasprilla, A.J., Martinez, G.A., Lunelli, B.H., Jardini, A.L. and Filho, R.M., 2012. Poly-lactic acid synthesis for application in biomedical devices – a review. *Biotechnology Advances,* 30(1), pp. 321–328.

Leukers, B., Gülkan, H., Irsen, S.H., Milz, S., Tille, C., Schieker, M. and Seitz, H., 2005. Hydroxyapatite scaffolds for bone tissue engineering made by 3D printing. *Journal of Materials Science: Materials in Medicine,* 16(12), pp. 1121–1124.

MakeItFrom, 2015. *Polylactic Acid (PLA, Polylactide)*. [online] Available at: <http://www.makeitfrom.com/material-properties/Polylactic-Acid-PLA-Polylactide> [Accessed September 2015].

Materialise, 2016a. *Fused Deposition Modeling*. [online] Available at: <http://manufacturing.materialise.com/fdm> [Accessed 16 June 2016].

Materialise, 2016b. *Laser Sintering*. [online] Available at: <http://manufacturing.materialise.com/laser-sintering-0> [Accessed 16 June 2016].

Materialise, 2016c. *Stereolithography*. [online] Available at: <http://manufacturing.materialise.com/stereolithography> [Accessed 16 June 2016].

MTS, 2015. *MTS Bionix® Tabletop Test Systems*. [pdf] Eden Prairie, MN: MTS Systems Corporation. Available at: <http://www.mts.com/ucm/groups/public/documents/library/dev_003992.pdf> [Accessed 1 October 2015].

Palermo, E., ed., 2013. What is Selective Laser Sintering? *Live Science*. [online] Available at: <http://www.livescience.com/38862-selective-laser-sintering.html> [Accessed 13 August 2013].

Pekarovicova, A., Chovancova-Lovell, V. and Fleming, P.D., 2006. Novel phase change inks for printing three-dimensional structures. *Journal of Imaging Science and Technology,* 50(6), pp.550–555.

Razak, S.I.A., Sharif, N.F.A. and Rahman, W.A.W.A., 2012. Biodegradable polymers and their bone applications: a review. *International Journal of Basic & Applied Sciences IJBAS IJENS,* 12(1), pp. 31–49.

Stoia, D.I., Vigaru, C. and Rusu, L., 2015. Laser sinterization aspects of PA2200 biocompatible powder – spinal cage application. *Key Engineering Materials*, 638, pp. 352–356.

Stratasys, 2016a. *PolyJet Technology*. [online] Available at: <http://www.stratasys.com/3d-printers/technologies/polyjet-technology> [Accessed February 2016].

Stratasys, 2016b. *ULTEM 9085 Resin*. [online] Available at: <http://www.stratasys.com/materials/fdm/~/media/83DA2BBEE7DE4A669CFEF6B1FCA118AA.ashx> [Accessed 16 June 2016].

Stratasys, 2016c. *Polyjet Materials Data Sheet*. [online] Available at: <http://usglobalimages.stratasys.com/Main/Files/Material_Spec_Sheets/MSS_PJ_PJMaterialsDataSheet.pdf?v=635785205440671440> [Accessed 16 June 2016].

Tao, C.T. and Young, T.H., 2006. Polyetherimide membrane formation by the cononsolvent system and its biocompatibility of MG63 cell line. *Journal of Membrane Science,* 269(1-2), pp. 66–74.

Test Standard Labs, 2016. *ABS Material Data Sheet*. [pdf] Dade City, FL: Test Standard Labs LLC. Available at: <http://teststandard.com/data_sheets/ABS_Data_sheet.pdf> [Accessed 16 June 2016].

Weisstein, E.W., 2016. Concave Function. *MathWorld – a Wolfram Web Resource*. [online] Available at: <http://mathworld.wolfram.com/ConcaveFunction.html> [Accessed December 2016].

Williams, J.M., Adewunmi, A., Schek, R.M., Flanagan, C.L., Krebsbach, P.H., Feinberg, S.E., Hollister S.J. and Das, S., 2005. Bone tissue engineering using polycaprolactone scaffolds fabricated via selective laser sintering. *Biomaterials,* 23(26), pp. 4817–4827.

Yahamed, A., Ikonomov, P. and Fleming, P.D., 2014. Application of 3D printing for human bone replacement. In: *Proceedings of the 2014 ICAM, International Conference on Advanced and Agile Manufacturing*, Rochester, MI., 28–30 May 2014. Norfolk, VA: International Society of Agile Manufacturing. p. 10.

Appendix A

Figures A1 to A5 show results of tensile strength tests for the materials printed at 100 % infill (ca is abbreviation for calculated).

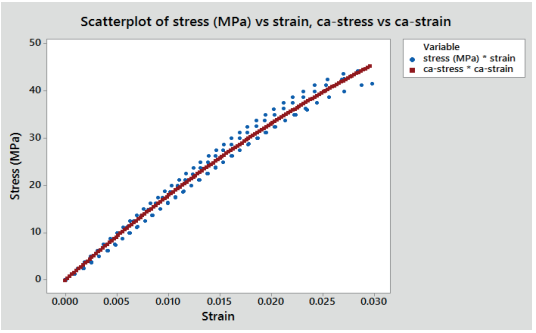

Figure A1: Measured and calculated stress-strain of ABS at 100 % infill

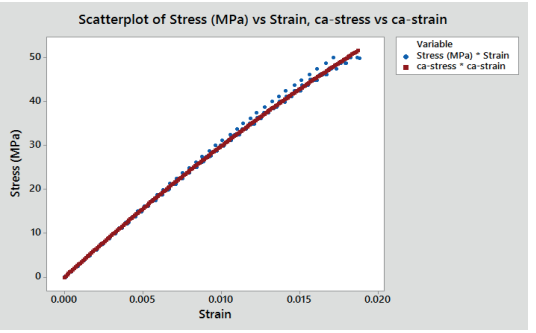

Figure A2: Measured and calculated stress-strain of PLA at 100 % infill

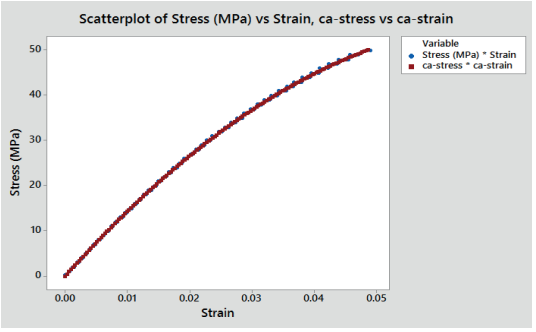

Figure A3: Measured and calculated stress-strain of ULTEM9085 at 100 % infill

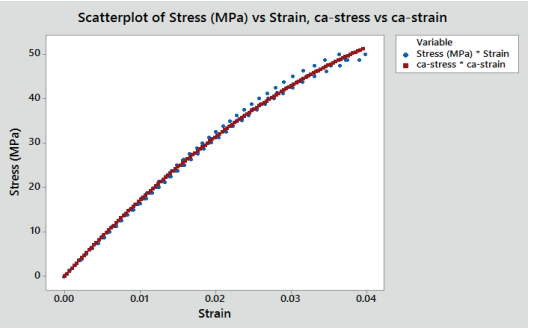

Figure A4: Measured and calculated stress-strain of PA2200 at 100 % infill

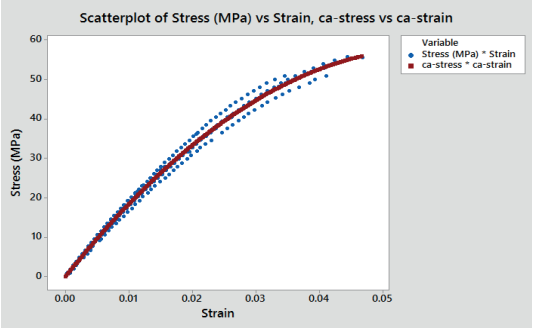

Figure A5: Measured and calculated stress-strain of Digital ABS™ at 100 % infill

Appendix B

Figures B1 to B8 show results of compressive tests in different directions for the materials printed at 100 % infill.

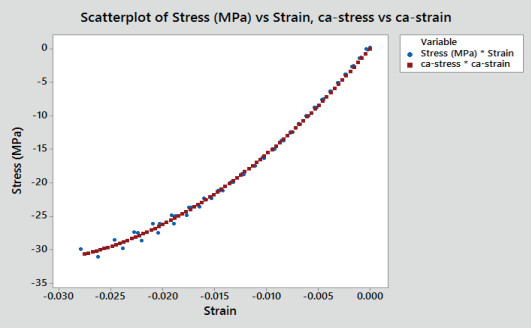

Figure B1: Measured and calculated stress-strain of ABS at 100 % infill in X direction

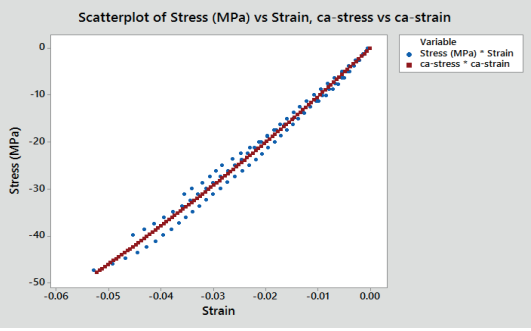

Figure B2: Measured and calculated stress-strain of ABS at 100 % infill in Z direction

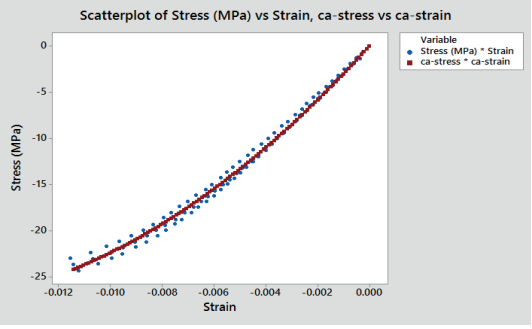

Figure B3: Measured and calculated stress-strain of PLA at 100 % infill in X direction

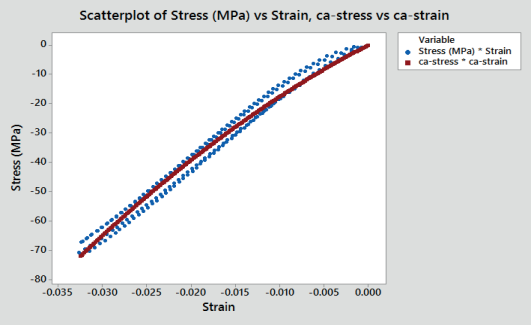

Figure B4: Measured and calculated stress-strain of PLA at 100 % infill in Z direction

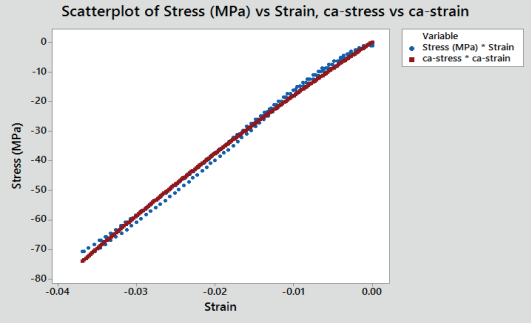

Figure B5: Measured and calculated stress-strain of Digital ABS™ at 100 % infill in X direction

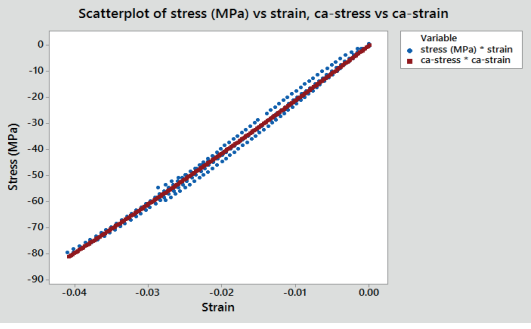

Figure B6: Measured and calculated stress-strain of Digital ABS™ at 100 % infill in Z direction

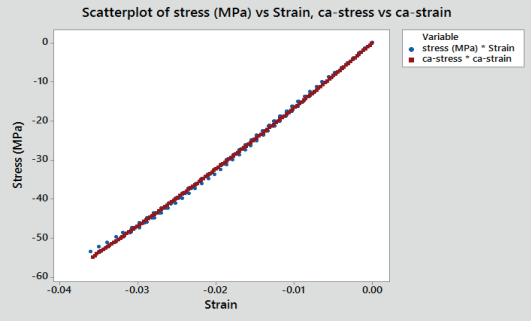

Figure B7: Measured and calculated stress-strain of ULTEM9085 at 100 % infill in X and Z directions

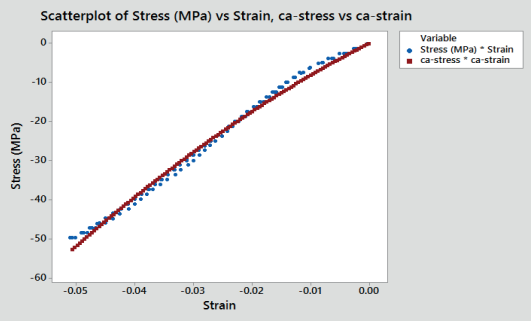

Figure B8: Measured and calculated stress-strain of PA2200 at 100 % infill in X and Z directions

Appendix C

Figures C1 to C5 show results of bending tests for the materials printed at 100 % infill.

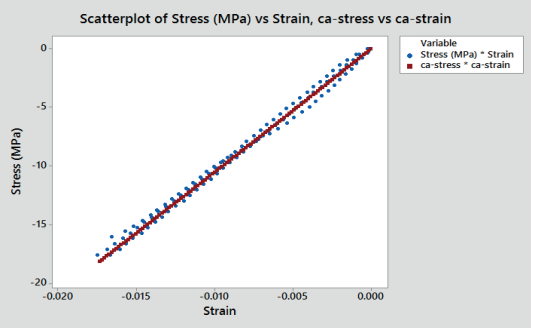

Figure C1: Measured and calculated stress-strain of ABS at 100 % infill

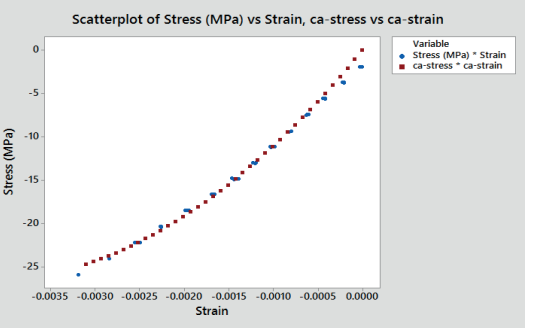

Figure C2: Measured and calculated stress-strain of PLA at 100 % infill

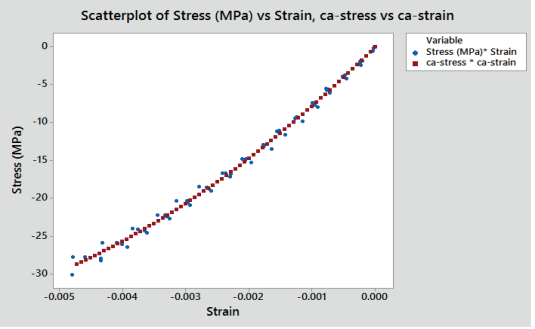

Figure C3: Measured and calculated stress-strain of ULTEM9085 at 100 % infill

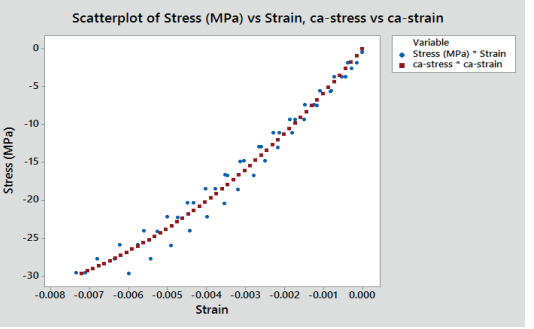

Figure C4: Measured and calculated stress-strain of PA2200 at 100 % infill

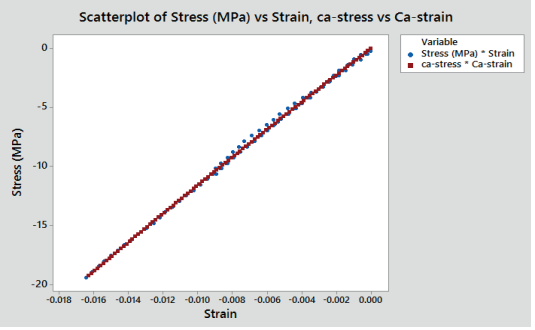

Figure C5: Measured and calculated stress-strain of Digital ABS™ at 100 % infill

Appendix D

Figures D1 to D6 show results of compressive tests for ABS cubes printed at 100 % infill at two different speeds 0.2 mm/s and 0.05 mm/s.

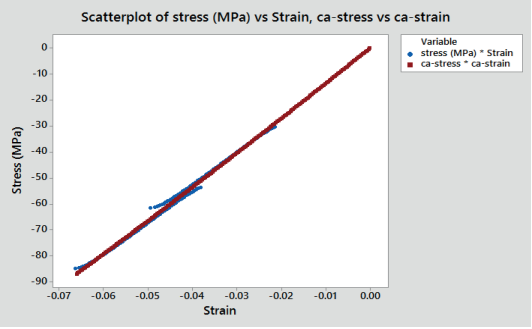

Figure D1: Measured and calculated stress-strain of ABS cube at 100 % infill for high strain in X direction at speed of 0.2 mm/s

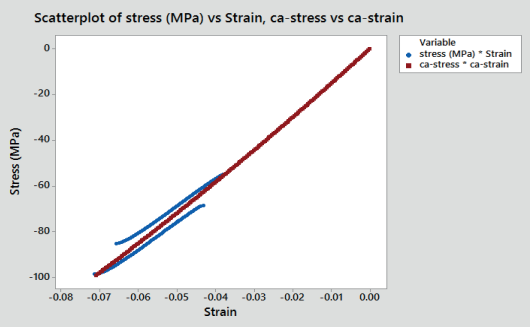

Figure D2: Measured and calculated stress-strain of ABS cube at 100 % infill for high strain in Y direction at speed of 0.2 mm/s

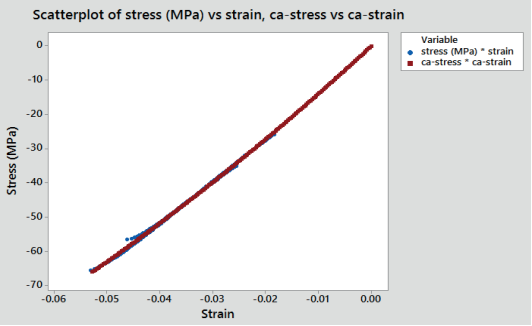

Figure D3: Measured and calculated stress-strain of ABS cube at 100 % infill for high strain in Z direction at speed of 0.2 mm/s

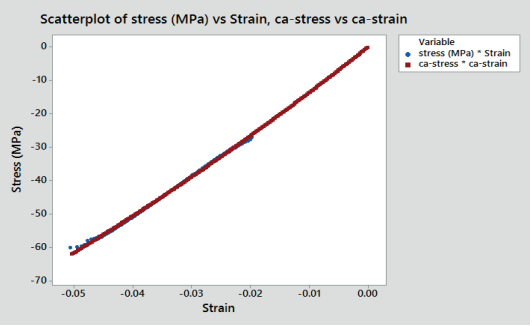

Figure D4: Measured and calculated stress-strain of ABS cube at 100 % infill for high strain in X direction at speed of 0.05 mm/s

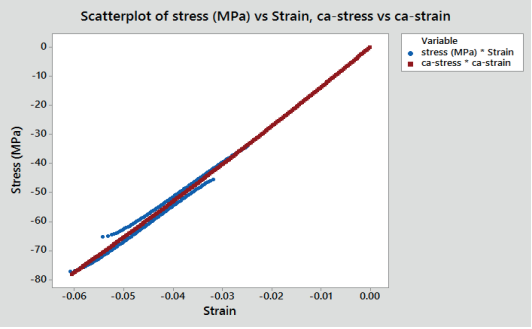

Figure D5: Measured and calculated stress-strain of ABS cube at 100 % infill for high strain in Y direction at speed of 0.05 mm/s

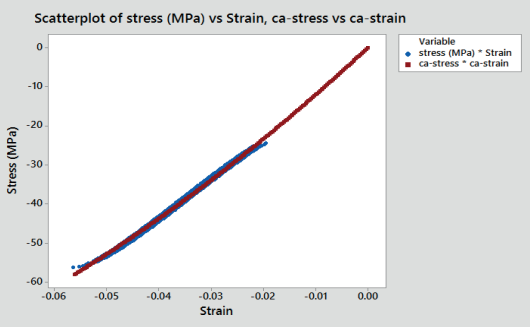

Figure D6: Measured and calculated stress-strain of ABS cube at 100 % infill for high strain in Z direction at speed of 0.05 mm/s